

# Structure and Transport Properties of a Plastic Crystal Ion Conductor: Diethyl(methyl)(isobutyl)phosphonium Hexafluorophosphate

Liyu Jin,<sup>†,§</sup> Kate M. Nairn,<sup>†,§</sup> Craig M. Forsyth,<sup>‡</sup> Aaron J. Seeber,<sup>||</sup> Douglas R. MacFarlane,<sup>‡,§</sup> Patrick C. Howlett,<sup>§,⊥</sup> Maria Forsyth,<sup>§,⊥</sup> and Jennifer M. Pringle<sup>\*,†,‡,§</sup>

<sup>†</sup>Department of Materials Engineering, and <sup>‡</sup>School of Chemistry, Monash University, Clayton, Victoria 3800, Australia

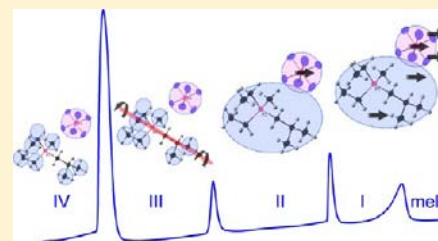
<sup>§</sup>ARC Centre of Excellence for Electromaterials Science

<sup>||</sup>CSIRO Process Science & Engineering, Private Bag 33, Clayton South, Victoria 3169, Australia

<sup>⊥</sup>Institute for Frontier Materials, Deakin University, Burwood Campus, Burwood, Victoria 3125, Australia

## Supporting Information

**ABSTRACT:** Understanding the ion transport behavior of organic ionic plastic crystals (OIPCs) is crucial for their potential application as solid electrolytes in various electrochemical devices such as lithium batteries. In the present work, the ion transport mechanism is elucidated by analyzing experimental data (single-crystal XRD, multinuclear solid-state NMR, DSC, ionic conductivity, and SEM) as well as the theoretical simulations (second moment-based solid static NMR line width simulations) for the OIPC diethyl(methyl)(isobutyl)phosphonium hexafluorophosphate ( $[P_{1,2,2,4}][PF_6]$ ). This material displays rich phase behavior and advantageous ionic conductivities, with three solid–solid phase transitions and a highly “plastic” and conductive final solid phase in which the conductivity reaches  $10^{-3} \text{ S cm}^{-1}$ . The crystal structure shows unique channel-like packing of the cations, which may allow the anions to diffuse more easily than the cations at lower temperatures. The strongly phase-dependent static NMR line widths of the  $^1\text{H}$ ,  $^{19}\text{F}$ , and  $^{31}\text{P}$  nuclei in this material have been well simulated by different levels of molecular motions in different phases. Thus, drawing together of the analytical and computational techniques has allowed the construction of a transport mechanism for  $[P_{1,2,2,4}][PF_6]$ . It is also anticipated that utilization of these techniques will allow a more detailed understanding of the transport mechanisms of other plastic crystal electrolyte materials.



## 1. INTRODUCTION

Plastic crystalline fast-ion conductors represent a unique family of materials with demonstrated merits as solid-state electrolytes for lithium rechargeable batteries,<sup>1–11</sup> fuel cells,<sup>12–16</sup> and dye-sensitized solar cells (DSSC).<sup>17–19</sup> Ionic compounds in which plastic phases are observed, termed “organic ionic plastic crystals” (OIPCs), are a recently developed subset of this family that offer important properties as electrolytes as a result of their nonflammability and negligible vapor pressure, unlike molecular plastic crystals.<sup>20</sup> The macroscopic transport properties of these materials (such as conductivity) have their origins in the molecular motions that occur as a result of the solid–solid phase changes. Understanding these motions is crucial to the development of OIPCs as electrolyte materials, but is also very challenging.

Plastic crystals are generally characterized by a low entropy of fusion ( $<20 \text{ J K}^{-1} \text{ mol}^{-1}$ )<sup>21</sup> and have the unique property of maintaining their long-range ordered crystalline lattice through one or more solid–solid phase transitions that introduce only short-range disorder. The disorder involved is typically associated with rotational and/or orientational changes in the molecules or ions.<sup>20,22</sup> As a consequence of this disorder, not only is fast-ion transport induced for either the matrix ions or doped targeted ions such as  $\text{Li}^+$ ,<sup>4</sup>  $\text{H}^+$ ,<sup>12</sup> or  $\text{I}^-/\text{I}_3^-$ ,<sup>23</sup> but also plastic mechanical properties are conferred; the materials are

often soft and waxy at ambient temperature.<sup>24</sup> Both of these properties are highly favorable for solid electrolytes, by (i) enabling good ionic conductivity, (ii) allowing the contact between the electrolyte and the electrodes to be maintained over a range of operating temperatures, and (iii) potentially allowing the fabrication of flexible devices such as DSSCs on plastic substrates.

Although molecular plastic crystals have been known since the 1960s, plasticity in organic ionic materials is a more recent discovery, and understanding of the transport and phase behavior of these materials is still in its infancy. Ikeda et al.<sup>25–27</sup> reported OIPCs based on quaternary alkylammonium cations with highly symmetric anions in the late 1980s, and in 1999 we reported a new family of OIPCs utilizing the pyrrolidinium cation.<sup>28</sup> In the latter family, the pyrrolidinium ring rotates easily, although the interionic interactions are sufficiently strong to maintain a crystalline structure. Since their original discovery, a large number of pyrrolidinium cation based OIPCs have been described. Alarco et al.<sup>29,30</sup> have studied pyrazolium-based OIPCs, and, through conductivity measurements, suggest that pipe diffusion is the dominant transport mechanism in these systems.<sup>30</sup>

Received: February 13, 2012

Published: May 29, 2012

However, quantitative and comprehensive information about the transport properties of this family of materials is rare, particularly for those that have multiple solid phases that often result in a change in transport behavior.<sup>20</sup> In principle, X-ray crystal structure data can allow the prediction of NMR line widths resulting from various types of reorientational and rotational motion in the crystalline lattice and hence reveal, by comparison with measured spectra, the motions present in each phase. However, the calculation task required for the line width prediction is nontrivial when the crystal structure involved is complex (e.g., large nonsymmetrical ions, more than one asymmetric unit per unit cell, multiple interacting nuclei types, etc). As discussed further below, early work in this direction investigated the motion of a symmetrical cation  $\text{Et}_4\text{N}$  in an  $\text{N}(\text{CN})_2$  salt and developed the method for this simpler case. In recent work, we have demonstrated the successful application of more complex OIPCs in a number of electrochemical contexts including lithium batteries,<sup>11</sup> dye-sensitized solar cells,<sup>17</sup> and proton conductors<sup>16</sup> for fuel cells. Thus, in line with these expanding applications, there is an increasingly urgent need to more fully understand the nature and origins of the transport and phase behavior in these promising materials.

In the present work, one of these new OIPCs, diethyl-(methyl)(isobutyl)phosphonium hexafluorophosphate,  $[\text{P}_{1,2,2,4}][\text{PF}_6]$ ,<sup>31</sup> has been chosen as an ideal example in which to more fully examine the ion transport properties associated with its crystal structure and different solid phases. The selection of this material is based on the following factors. First, this compound contains three NMR-friendly nuclei,  $^1\text{H}$ ,  $^{19}\text{F}$ , and  $^{31}\text{P}$ , so that NMR line width and diffusion characterization can be used to provide comprehensive information on the molecular motions of both cations and anions. Second, this is a typical OIPC, exhibiting multiple well-defined solid–solid phase transitions and an entropy of fusion of only  $5 \text{ J K}^{-1} \text{ mol}^{-1}$ . Finally, we have successfully analyzed its crystal structure using single-crystal X-ray diffraction; it is usually very difficult to obtain good crystallographic data for OIPCs as it is hard to totally “freeze” the short-range disorder under ambient or even cryogenic conditions. Thus, a transport model for  $[\text{P}_{1,2,2,4}][\text{PF}_6]$  has been compiled using single crystal X-ray diffraction analysis, differential scanning calorimetry (DSC), impedance spectroscopy, and variable-temperature solid-state NMR line width and diffusion data. Moreover, this transport model has been tested by comparing the experimentally obtained NMR line widths with those obtained from second moment calculations for various ionic motions; this comparison has allowed us to model the evolution of the molecular motions in each phase.

## 2. EXPERIMENTAL SECTION

**2.1. Preparation of  $[\text{P}_{1,2,2,4}][\text{PF}_6]$ .**  $[\text{P}_{1,2,2,4}][\text{PF}_6]$  was prepared as described elsewhere.<sup>31</sup> Potassium hexafluorophosphate was added to diethyl(methyl)(isobutyl)phosphonium tosylate in distilled water, immediately forming the product as a white precipitate. The precipitate was isolated by filtration, washed several times with distilled water, and dried under vacuum for several days at  $100^\circ\text{C}$ .

**2.2. Differential Scanning Calorimetry (DSC).** DSC was performed with a TA-Q100 instrument. All samples were weighed and sealed in aluminum pans under  $\text{N}_2$  atmosphere. The samples were first cooled from room temperature to  $-30^\circ\text{C}$ , and subsequently heated to  $170^\circ\text{C}$  at a rate of  $2^\circ\text{C}/\text{min}$ . The first run was performed to remove the effects of thermal history of the samples. A second repeat cooling and heating cycle was carried out and used to obtain the phase transition temperatures and other parameters presented here.

**2.3. AC Impedance Spectroscopy.** The ionic conductivity of all samples was measured by ac impedance spectroscopy using a frequency response analyzer (Solartron FRA 1296), driven by Solartron impedance measurement software. The powder samples were first pressed into pellets (1 mm thick and 13 mm in diameter) using a KBr die and a hydraulic press at 10 ton for 30 min; then they were sandwiched between two stainless steel blocking electrodes. Both preliminary pressing and blocking-electrode cell testing were performed under hermetic protection. Data were collected over a frequency range from 10 MHz to 1 Hz using a signal voltage of 0.1 V at temperatures ranging from 0 to  $130^\circ\text{C}$  at  $5^\circ\text{C}$  intervals. The cell temperature was controlled using a Eurotherm controller (model 2204), and the temperature was measured to within  $1^\circ\text{C}$  using a thermocouple type T, which was attached to one blocking electrode. The ramp rate used was approximately  $0.33^\circ\text{C}/\text{min}$ , and the sample was held for a short equilibration time, up to 2 min, to stabilize the temperature prior to impedance measurement.

**2.4. Single-Crystal X-ray Diffraction.** As a result of the inherent rotational or orientational disorder, a single crystal of  $[\text{P}_{1,2,2,4}][\text{PF}_6]$  grown under ambient conditions and quenched to 123 K gave a very poor diffraction pattern. Thus, to obtain a fully ordered lattice, the crystals were grown at 250 K, then transferred by cryoloop and immediately frozen to 123 K on the diffractometer. X-ray diffraction data were collected at 123(1) K on an Oxford Gemini CCD diffractometer using  $\text{Mo K}\alpha$  radiation ( $\lambda = 0.71073 \text{ \AA}$ ) and processed using CrysAlisPro software (Version no.: 1.171.34.36, Agilent Technologies). The final specimen comprised an irregular colorless block-shaped crystal of approximate dimensions  $0.25 \times 0.25 \times 0.25 \text{ mm}$ . Data were collected to  $2\theta_{\text{max}}$  of  $64.9^\circ$  yielding 18 699 reflections ( $I_p$  and multiscan absorption corrections applied). The structure was solved and refined with SHELX-97<sup>32</sup> using 4729 unique reflections ( $R_{\text{int}} = 0.027$ ) of which 3684 have  $I > 2\sigma I$ . All non-hydrogen atoms were refined with anisotropic thermal parameters; hydrogen atoms were placed in calculated positions using a riding model with  $\text{C-H} = 0.98\text{--}1.00 \text{ \AA}$  and  $U_{\text{iso}}(\text{H}) = 1.2U_{\text{iso}}(\text{C})$  or  $1.5U_{\text{iso}}(\text{C})$ .

**2.5. Scanning Electron Microscopy.** A JEOL 7001F SEM was used for morphology analysis. The scanned surfaces shown were cross sections of fractured pellets prepared by uniaxial pressing of the sample powder. All images were acquired with an accelerating voltage of 5.0 kV and probe current of 1.0 nA.

**2.6. Solid-State NMR Line Width and Diffusion Measurements.** Both line width and diffusion measurements were performed using the same sample of fine powder, which had been packed and sealed under nitrogen in a 5 mm Schott E NMR tube.  $^1\text{H}$ ,  $^{31}\text{P}$ , and  $^{19}\text{F}$  NMR line width measurements were performed on a Bruker Avance 300 pulsed NMR spectrometer operating at Larmor frequencies of 300.13, 121.49, and 282.41 MHz, respectively. A Diff30 diffusion probe was used for all experiments. Both  $^1\text{H}$  and  $^{19}\text{F}$  line width spectra were acquired using single pulses of 6  $\mu\text{s}$ , recycle delays of 5 s, and 256 scans.  $^{31}\text{P}$  line width spectra were acquired using a single pulse of 6.5  $\mu\text{s}$ , a recycle delay of 10 s, and 256 scans. The sample temperatures were controlled by heating against a stream of cold nitrogen gas for temperatures between 180 and 293 K and a stream of air for temperatures between 303 and 403 K. Measured sample temperatures were calibrated using neat ethylene glycol based on a literature method.<sup>33</sup> Line width fitting was carried out using the software package Dm2009 (Version no.: 20090330).<sup>34</sup> Solid-state diffusion measurements were performed using a pulse-field-gradient Stimulated Echo (PFG-STE) sequence, where the gradient strength was varied in 32 steps up to the highest gradient strength (1500 G/cm). To obtain sufficient signal-to-noise, 64 scans were taken at each gradient. For each scan, the gradient pulse length was set to 3 ms with variable diffusion time (20, 40, or 60 ms for different temperatures). The intensity versus gradient data were fitted to the Stejskal–Tanner equation<sup>35</sup> using the nonlinear least-squares method within the Bruker Topspin 2.1 software to obtain diffusion coefficients.

**2.7. Second Moment Calculation.** See the Supporting Information.

### 3. RESULTS AND DISCUSSION

**3.1. The Structure of  $[P_{1,2,2,4}][PF_6]$ .** *3.1.1. Single-Crystal Structure.* Single-crystal structure analysis (Tables S1–S6) indicates that the low temperature phase of  $[P_{1,2,2,4}][PF_6]$  belongs to the  $Pbca$  space group with orthorhombic parameters  $a = 12.9833(4)$  Å,  $b = 14.3872(4)$  Å,  $c = 15.1944(4)$  Å. There are eight equivalent  $[P_{1,2,2,4}][PF_6]$  ion pairs in a unit cell; one of them is shown in Figure 1.

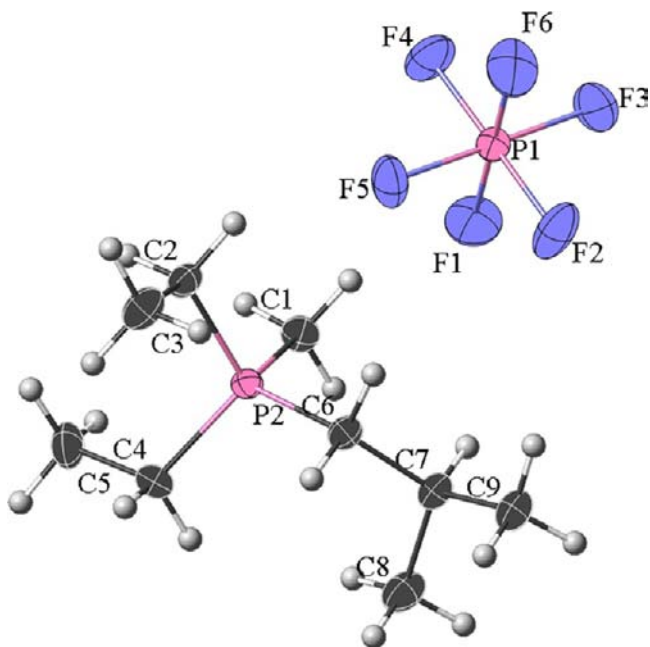


**Figure 1.** The structure of a  $[P_{1,2,2,4}][PF_6]$  ion pair as determined by X-ray diffraction.

Both the tetrahedral  $[P_{1,2,2,4}]$  cation and the octahedral  $PF_6^-$  anion are completely ordered. For the anion, the P–F bond distances of 1.5883(1)–1.6003(1) Å and  $U_{eq}$  values in the range 0.0387(2)–0.0536(3) Å are in agreement with those reported for the related salt  $[N(^{n}Bu)_4][PF_6]$  at 110 K<sup>36</sup> and for pyrrolidinium hexafluorophosphate plastic crystals at 123 K.<sup>37</sup>

As shown in the extended lattice (Figure 2), each  $PF_6^-$  anion is surrounded by six  $[P_{1,2,2,4}]$  cations, with eight C–H···F contacts in the range 2.451–2.635 Å, at or marginally below the van der Waals separation ( $H\cdots F = 2.67$  Å).<sup>36</sup> As weak hydrogen bonds are generally defined as those with an  $H\cdots A$  ( $A =$  acceptor) length of  $>2.2$  Å,<sup>38</sup> these C–H···F contacts can be regarded as weak electrostatic or dispersion interactions, which are likely to allow rotational and orientational disorder of the anions and the alkyl chains of the cations. Interestingly, from the packing diagrams (Figure 2a and b), the butyl chains extend and interleave to form a “skeleton” along the  $b$  axis and the anions are aligned parallel to the  $b$  axis (Figure 2a). From the view of Figure 2b, the cation “skeleton” forms a channel-like structure to accommodate anions. However, with the filling of the anion, those “channels” are still considerably open, which may allow greater anion mobility as well as fast ion conduction of  $Li^+$  if doped with a lithium salt such as  $LiPF_6$ .

*3.1.2. Microstructure.* In sharp contrast to normal inorganic ionic crystals like sodium chloride, which are hard and brittle, the microstructure of  $[P_{1,2,2,4}][PF_6]$  shows strong evidence of plasticity. The SEM images (Figure 3) show selected regions of the fracture surface of a  $[P_{1,2,2,4}][PF_6]$  pellet prepared by uniaxial pressing of the powder. Several grains with different orientations can be observed, with ridge-like grain boundaries. A single grain can experience strong compressive stresses, transmitted via the surrounding grains during uniaxial pressing, and these stresses can be dissipated in two ways: plastic deformation or brittle fracture. In Figure 3a the major stress dissipation mechanism appears to be plastic deformation, as many sets of slip planes within different grains can be seen. It is clear that sets of slip steps retain their coherency until they meet grain boundaries. Figure 3b shows a more distinct slip phenomenon. These predominant plastic deformations are also observed in other plastic crystal systems;<sup>39,40</sup> however,  $[P_{1,2,2,4}][PF_6]$  appears “softer” as compared to some pyrrolidinium plastic crystals, which show brittle features and sharp edges on their fracture surfaces.<sup>40</sup>

These easily activated plastic deformations are largely attributed to the inherent short-range rotational disorder embedded in a long-range ordered crystalline structure. This disorder can effectively reduce the energy barriers for initiating

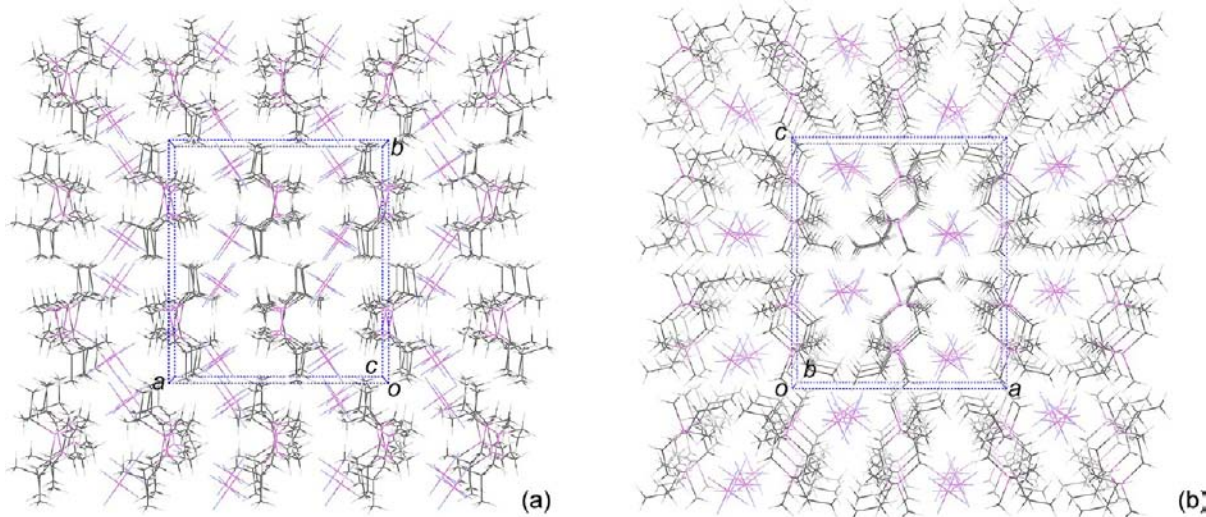
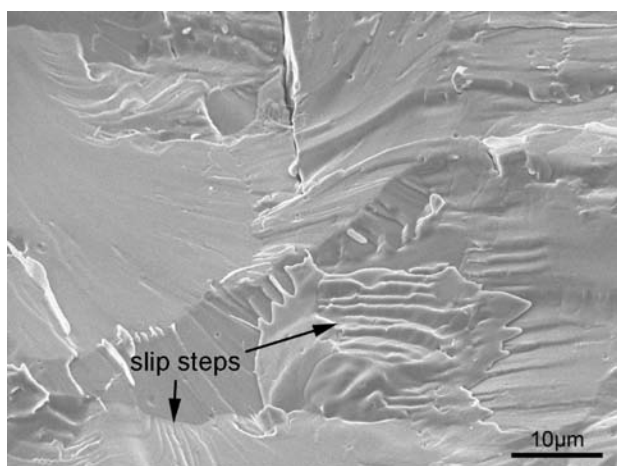
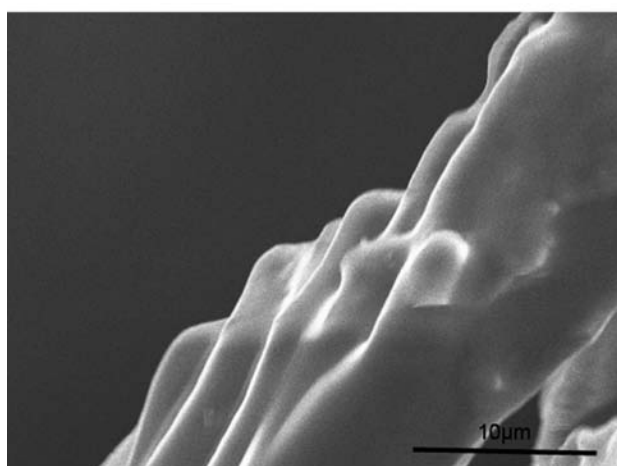


**Figure 2.** The extended crystal structure packing viewed along the  $c$  direction (a) and  $b$  direction (b).



(a)



(b)

**Figure 3.** Microstructures of featured areas of the fracture surface of  $[P_{1,2,2,4}][PF_6]$  (sample was prepared and images captured at room temperature).

dislocation motion by weakening the inter- and intramolecular interactions and forming vacancies.<sup>24</sup> The high plasticity of  $[P_{1,2,2,4}][PF_6]$  implies relatively easy motion of cations and anions within the material, which is consistent with the relatively open structure shown in Figure 2.

**3.2. Thermal Properties and Ionic Conductivity.** We have recently reported both DSC and ionic conductivity of this material (without detailed discussion) in a paper reporting the first synthesis of a range of phosphonium-based ionic liquids and plastic crystals.<sup>31</sup> For the detailed analysis reported here, the material was freshly synthesized and the ionic conductivity was measured by a different method (using a pellet barrel cell rather than a dip cell, see section 2.3). The updated DSC trace and ionic conductivity of  $[P_{1,2,2,4}][PF_6]$  are plotted in Figure 4.

**3.2.1. Thermal Properties.** Three distinct solid–solid transition peaks were observed in the DSC trace, which differentiate four solid phases (following the phase nomenclature system described elsewhere, where the highest temperature solid phase is denoted phase I<sup>41</sup>) before the melt at 150 °C. The solid–solid phase transitions are consistent with those reported previously,<sup>31</sup> while the slightly higher melting point reported here is most likely a reflection of the different thermal histories of the samples, as OIPCs are known to exhibit metastability.<sup>42</sup> There are no thermal transitions between –130

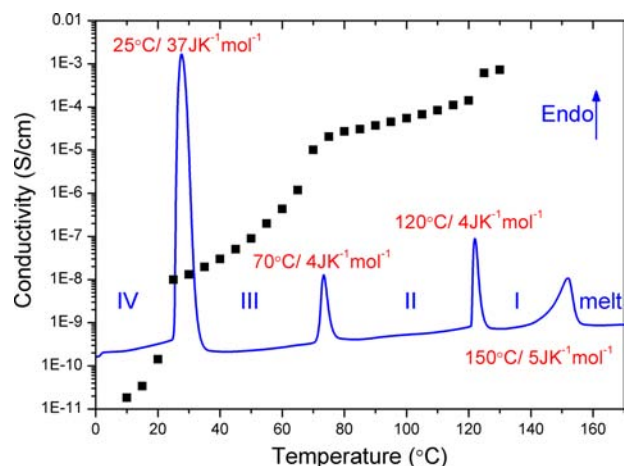


**Figure 4.** The DSC trace (second heating cycle) of  $[P_{1,2,2,4}][PF_6]$  and the conductivity as a function of temperature. Each solid phase is labeled by Roman numerals, and the peak temperatures and entropy changes for each phase transition are given.

and 25 °C.<sup>31</sup> The first (lowest temperature) phase transition at 25 °C is the strongest, with 74% of the total taken up, after which a particularly broad temperature range of the plastic phase is observed, ideal for ambient and moderate-temperature applications of the material. The second and third solid–solid transitions involve relatively low entropy changes, only 4 and 5  $J K^{-1} mol^{-1}$ , respectively. It is interesting to note that the melting peak is reproducibly broad; we speculate that voids or vacancies in the lattice can act as “dopants”, which effectively broaden the melting peak. This is supported by the fact that a significant volume expansion (vacancy formation) upon the final solid–solid phase transition has been observed for the OIPC tetraethylammonium dicyanamide,<sup>43</sup> which then also shows a similarly broad melting peak. We regard phase I of  $[P_{1,2,2,4}][PF_6]$  as a material with a high concentration of vacancies, which is also indicated by the fact that the entropy change of the melting transition is only 5  $J K^{-1} mol^{-1}$ , indicating significant disorder in the material in phase I and far below the 20  $J K^{-1} mol^{-1}$  required by Timmerman’s criterion for plastic crystalline behavior.<sup>21</sup>

The nature of these solid transitions is more complex than those observed in metals or ceramics,<sup>44</sup> where lattice space group transformations are the main cause of endothermic processes. In contrast, for plastic crystals, within the same or slightly expanded lattice, onset of rotational motions of particular parts of the molecules often accounts for the solid–solid phase transitions.<sup>37,45,46</sup> Lattice space group transformations have been observed by variable-temperature X-ray powder diffraction of *N,N*-dimethylpyrrolidinium tetrafluoroborate ( $[C_1mpyr][BF_4]$ )<sup>47</sup> and bis(*N*-hexylimidazolium) hexafluorophosphate.<sup>48</sup> However, for the  $[P_{1,2,2,4}][PF_6]$  material, it is more likely that the phase transitions are due to the onset of particular rotational motions, rather than lattice transformations, as suggested by the ionic conductivity data (Figure 4), which show orders of magnitude increases in conductivity at each phase transition, especially for the phase IV to III transition. This step change in ionic conductivity is likely facilitated by the shift from a more “rigid” phase to a highly disordered phase, which is also consistent with the NMR line width measurements, as shown later.

**3.2.2. Ionic Conductivity.** The ionic conductivity of  $[P_{1,2,2,4}][PF_6]$  significantly increases with temperature and

jumps at each solid–solid transition (Figure 4), reaching 1 mS/cm in phase I. To examine the phase-dependent ionic conductivity behavior more quantitatively, the Arrhenius activation energies ( $E_a$ ) for each phase were calculated<sup>49</sup> from  $\sigma = \sigma^0 \exp(-E_a/(k_B T))$  (where  $\sigma$  is ionic conductivity,  $\sigma^0$  is a pre-exponential factor,  $E_a$  is activation energy,  $T$  is temperature in Kelvin) and are listed in Table 1. Even the highest activation

**Table 1. Arrhenius Activation Energies for Conduction,  $E_a$ , in Each Phase**

phase	IV	III	II	I <sup>a</sup>
$E_a$ (kJ mol <sup>-1</sup> )	74 ± 6	43 ± 3	20 ± 1	

<sup>a</sup>Insufficient data for phase I.

energy, in phase IV, is relatively small as compared to activation energies of other OIPC systems.<sup>48,50</sup> In moving from phase IV through to II, the dramatic reduction in  $E_a$  evidences the highly phase-dependent transport properties of this material. The activation energy in phase II is more characteristic of an ionic liquid. The motions of ions in phases III and II are less hindered than in phase IV; that is, the ions require less energy to pass one another. The disordering or rotational motion involved in these phases creates vacancies, which facilitate the motion of ions, as suggested by Shimizu et al. for di-*n*-alkylammonium bromide plastic crystals.<sup>46</sup> Therefore, in the highly disordered phases of  $[P_{1,2,2,4}][PF_6]$ , the conductivity goes up to around 10<sup>-4</sup> S cm<sup>-1</sup> in phase II and 10<sup>-3</sup> S cm<sup>-1</sup> in phase I. The material thus displays liquid-like conductivities well below the final melt of the material. The decrease in  $E_a$  from phase IV to II, with corresponding increases in conductivity, demonstrates the importance of the specific molecular motions

taking place in each phase, which we have further examined using in-depth solid-state NMR analysis.

**3.3. Solid-State NMR Characterization. 3.3.1. <sup>1</sup>H and <sup>19</sup>F NMR Line Width and Diffusion Measurements.** As the disorder in plastic crystal materials generally prohibits the resolution of single-crystal X-ray diffraction patterns at room temperature, solid-state NMR analysis is an extremely valuable analytical tool for assessing the interactions within these materials. The short-range disorder can significantly affect the dipole–dipole interactions (both intramolecular<sup>51</sup> and even some intermolecular interactions), which can be effectively detected by single-pulse static NMR measurements.<sup>52</sup>

As <sup>1</sup>H is only present in the cation of  $[P_{1,2,2,4}][PF_6]$ , and <sup>19</sup>F exists only in the anion, they allow convenient differentiation of the motions of the cation and the anion. Here, we use the line width at half-maximum of the peak (denoted line width below) to characterize the extent of the molecular motions.<sup>51</sup> <sup>1</sup>H and <sup>19</sup>F spectra as a function of temperature are shown in Figure 5. The high temperature diffusion coefficients, and the fractions of second narrow peaks for both <sup>1</sup>H and <sup>19</sup>F, are plotted as functions of temperature in Figures 6 and 7, respectively. For <sup>1</sup>H, within phase IV (193–293 K), the line width drops from 48 to 36 kHz. The line width decreases significantly to ca. 12 kHz when the system enters phase III (303 K). Interestingly, the line widths in phase III (303–343 K) are reasonably constant with increasing temperature. A second narrow peak (with a line width of ca. 700 Hz) on top of the initial broad peak becomes distinguishable from 333 K, suggesting that there is a small but growing proportion of diffusive cations present in the higher temperatures of phase III. This is confirmed by the presence of

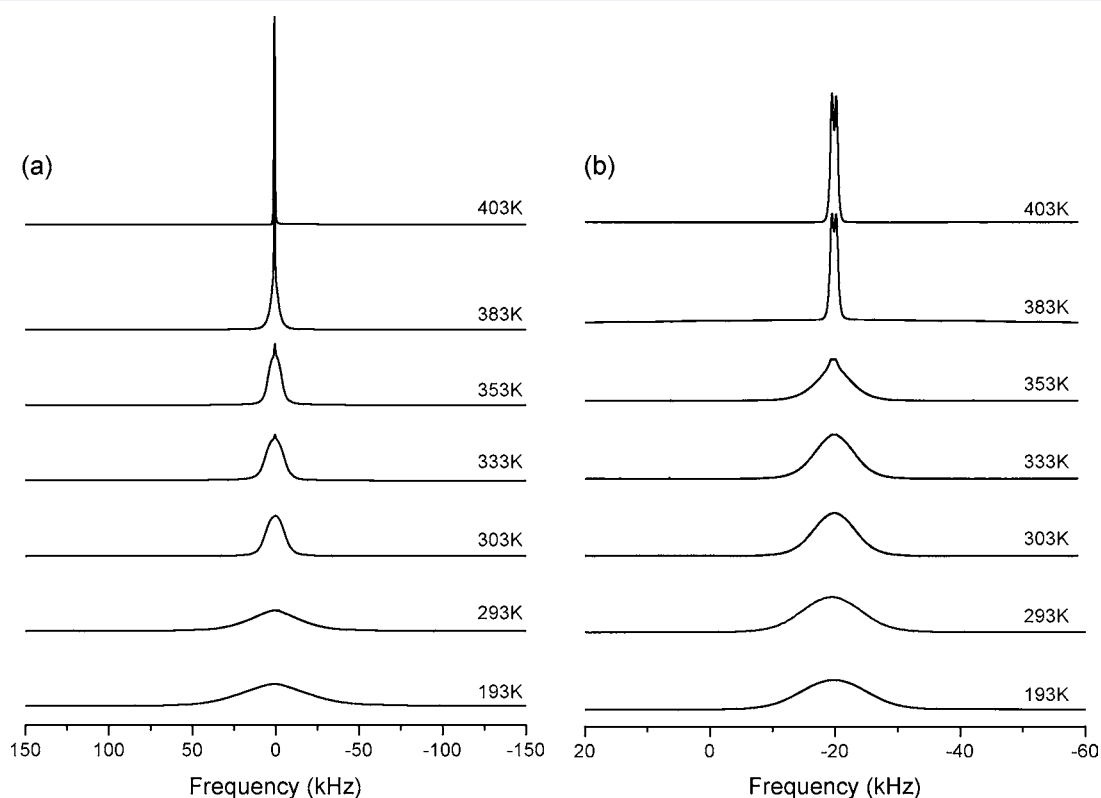


**Figure 5.** (a) Selected <sup>1</sup>H single-pulse spectra versus temperature and (b) selected <sup>19</sup>F single-pulse spectra versus temperature. In phase II, a dramatic reduction in line width allows a doublet in the <sup>19</sup>F spectra to be observed; this is from the F–P  $J$ -coupling, where  $J_{PF} =$  ca. 720 Hz.

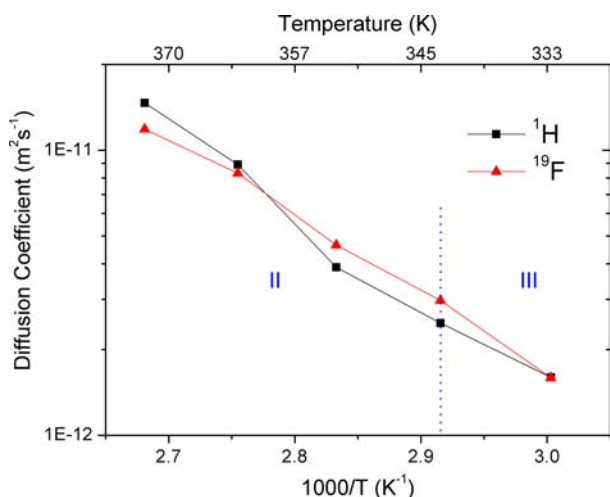


**Figure 6.** Diffusion coefficients of  $^1\text{H}$  (i.e., cation) and  $^{19}\text{F}$  (i.e., anion) as functions of temperature. The blue dashed line separates phase III and phase II (as determined by DSC).

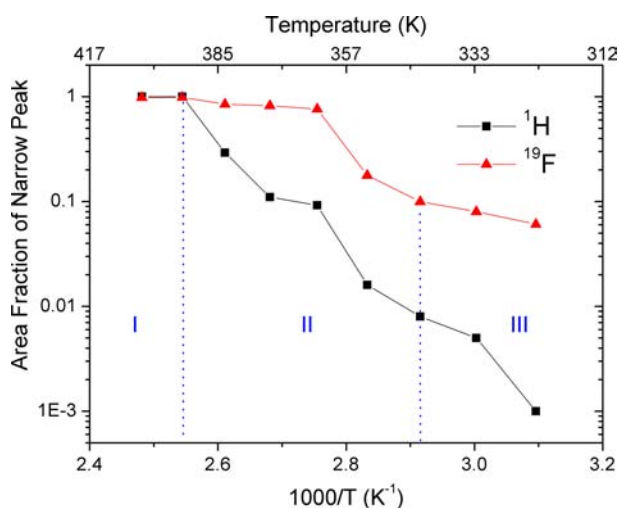


**Figure 7.** Area fractions of narrow peaks (peak 2) for  $^1\text{H}$  and  $^{19}\text{F}$  as functions of temperature, obtained from deconvolution of the  $^1\text{H}$  and  $^{19}\text{F}$  static NMR spectra. The blue dashed lines separate different phases, as determined by DSC.

measurable  $^1\text{H}$  diffusion coefficients from 333 K, as shown in Figure 6.

Within phase II (353–383 K), the peaks gradually narrow again with increasing temperature, accompanied by a dramatic growth in the proportion of diffusive cations (Figure 7) and enhanced diffusion coefficients (Figure 6). In phase I (403 K), the original broad peak has totally disappeared, leaving only the narrow peak (ca. 700 Hz), suggesting that the vast majority of cations have translational motion at this temperature. The evolution of line widths for fluorine is similar to that of the protons (Figure 7). However, from 363 K almost all fluorines are highly mobile (probably diffusive) with line widths of only ca. 600 Hz. As the temperature further increases into the phase I regime (403 K), no further line width narrowing is observed. The diffusion coefficients of both cation and anion in phase II (Figure 6) are similar, and increase to  $10^{-11} \text{ m}^2 \text{ s}^{-1}$  at 373 K, which is close to both  $^1\text{H}$  and  $^{19}\text{F}$  diffusion coefficients measured in  $[\text{C}_3\text{mpyr}][\text{NTf}_2]$  at room temperature.<sup>53</sup>

**3.3.2.  $^{31}\text{P}$  NMR Line Width Measurements.** Phosphorus is the central atom of both the cation and the anion (Figure 1), and correspondingly the  $^{31}\text{P}$  NMR spectra (Figure 8) show two

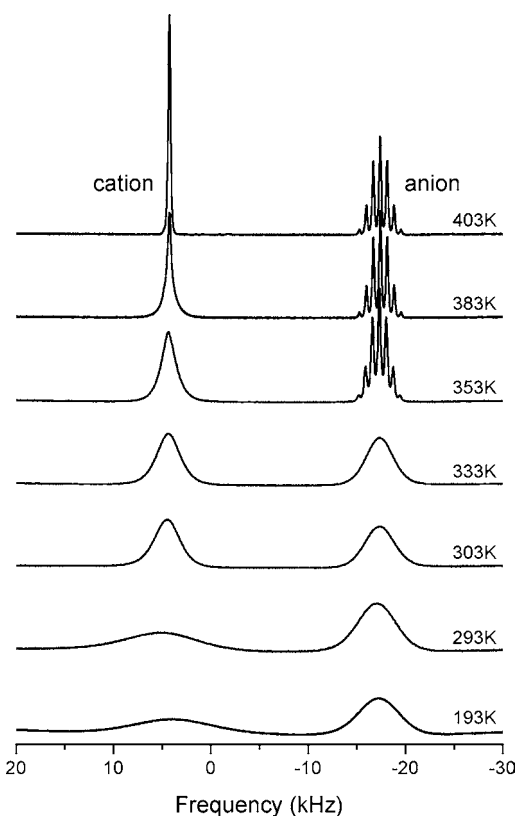


**Figure 8.** The evolution of selected single-pulse  $^{31}\text{P}$  spectra versus temperature. The multiplet from the anion is observed from phase II (353 K) with  $J_{\text{PF}} = \text{ca. } 720 \text{ Hz}$ , consistent with the  $^{19}\text{F}$  NMR spectra (Figure 5).

distinct chemical shifts. The changes in line width of the  $^{31}\text{P}$ -cation and  $^{31}\text{P}$ -anion peaks as a function of temperature are in good agreement with those of the  $^1\text{H}$  and  $^{19}\text{F}$  cation and anion peaks (Figure 5).

**3.4. Second Moment Line Width Simulations.** To relate the measured  $^1\text{H}$ ,  $^{19}\text{F}$ , and  $^{31}\text{P}$  NMR line widths for  $[\text{P}_{1,2,2,4}][\text{PF}_6]$  to different rotational processes within the plastic crystal, we can use atomic coordinates determined from the crystal structure to calculate expected line widths for the rotational processes and compare these to the experimentally measured values.<sup>46,54–56</sup> First, the theoretical rigid second moment ( $M_2$ ) calculation was carried out using the modified form<sup>54</sup> of Van Vleck's original equation:<sup>52</sup>

$$M_2 = \left(\frac{\mu_0}{4\pi}\right)^2 \frac{\hbar^2}{N} \left[ \frac{3}{5} \sum_{j,k} \gamma_k^4 I_k (I_k + 1) r_{jk}^{-6} + \frac{4}{15} \sum_{j,f} \gamma_j^2 \gamma_f^2 I_f (I_f + 1) r_{jf}^{-6} \right]$$

where  $N$  is the number of resonant nuclei covered by the finite 3D space used for  $M_2$  calculation (usually a block containing  $3 \times 3 \times 3 = 27$  unit cells or an isolated molecule),  $\mu_0$  is the vacuum permeability, and  $\hbar$  is the reduced Planck's constant. Nucleus  $j$  is the nucleus whose line width is calculated (e.g., a

proton); nuclei  $k$  are all the other nuclei of that species (e.g., the other protons); and nuclei  $f$  are all other NMR active nuclei within the unit cell (e.g., the phosphorus and fluorine).  $\gamma$  is the gyromagnetic ratio in  $\text{rad T}^{-1} \text{s}^{-1}$ .  $I$  is the spin quantum number, and  $r$  is the internuclear distance.

Next, for direct comparison with experimental data, the line width in hertz can be obtained from  $M_2$ :<sup>54</sup>

$$\Delta\nu_{\text{fwhm}} = \frac{\sqrt{2\ln(2)M_2}}{\pi}$$

Using this procedure, the second moment simulations and theoretical line widths for each solid phase of  $[\text{P}_{1,2,2,4}][\text{PF}_6]$  were calculated, as discussed below.

**Phase IV.** The theoretical line widths from the fully rigid structure (i.e., where all dipole–dipole interactions are present) are calculated for two different systems: (a) an isolated  $[\text{P}_{1,2,2,4}][\text{PF}_6]$  ion pair, and (b) one particular  $[\text{P}_{1,2,2,4}][\text{PF}_6]$  pair within the central unit cell of a  $3 \times 3 \times 3$  block of 27 unit cells to explore the effect of longer-range interactions. Both values are shown in Table 2.

**Table 2. Line Width Calculations for the Rigid Structure of  $[\text{P}_{1,2,2,4}][\text{PF}_6]$**

nucleus	calculated line widths/kHz			
	<sup>1</sup> H	<sup>19</sup> F	<sup>31</sup> P-cation	<sup>31</sup> P-anion
isolated	63.7	33.2	13.0	29.3
within a $3 \times 3 \times 3$ unit cell block	67.8	36.8	14.0	29.8

The calculated values for the  $[\text{P}_{1,2,2,4}][\text{PF}_6]$  in the block are all only slightly larger than those for the isolated  $[\text{P}_{1,2,2,4}][\text{PF}_6]$ , which indicates that the intraionic interaction and the interaction between the anion and cation in an individual unit provide the major contributions to the line widths of all three nuclei. However, the line widths measured (Figure 9) at the lowest experimental temperature (193 K) are already much smaller than these calculated values, especially for <sup>31</sup>P-anion (ca. 4.8 kHz) and <sup>19</sup>F (ca. 12.3 kHz). This indicates that at 193 K the structure is not fully rigid and some motion, at least of the anions, is present. There is probably negligible steric hindrance to the rotation of the  $\text{PF}_6^-$ , as suggested from the apparent free volume within the crystal structure (Figure 2). At 193 K, the cations are reasonably immobile, because the observed line widths for <sup>1</sup>H (ca. 46.7 kHz) and <sup>31</sup>P-cation (ca. 9.2 kHz) are around two-thirds of the values calculated for the fully rigid state.

In phase IV, as the temperature increases from 193 to 293 K, the observed line widths for <sup>19</sup>F, <sup>31</sup>P-anion, and <sup>31</sup>P-cation decrease by less than 10%. However, the <sup>1</sup>H line widths experience a more significant drop (ca. 33%). This suggests that isotropic reorientation of the methyl and/or ethyl groups has increased; the energy barriers for these rotations are relatively low (3.7 kJ/mol for those in glassy polymers<sup>57</sup>), so they are likely to occur at lower temperatures than other types of cation motion.<sup>58</sup> The second moment of <sup>1</sup>H in the presence of methyl and ethyl group rotation was calculated on the basis of the method of Gutowsky and Pake,<sup>59</sup> assuming that the rate of rotation is such that the maximum averaging of the <sup>1</sup>H–<sup>1</sup>H interactions takes place, and that the values of these interactions are reduced to 25% of their values in the rigid system. The calculation was performed on an isolated  $[\text{P}_{1,2,2,4}][\text{PF}_6]$ , and interactions between  $[\text{P}_{1,2,2,4}][\text{PF}_6]$  units were not taken into

account. The effect of anion tumbling was included in the calculation by collocating all six F atoms with the P of the anion (which represents the center of mass of the anion) and using these revised atomic positions to calculate the F–H interactions. The combination of methyl group rotation and anion tumbling reduced the calculated <sup>1</sup>H line width from 63.7 to 43.6 kHz. This value is in agreement with the observed value in the middle of phase IV (around 253 K), as shown in Figure 9a. When ethyl group rotation was incorporated, the calculated line width was between 39 and 35 kHz. The higher line width does not allow for any averaging of the interactions between the protons in the  $\text{CH}_2$  groups and the protons in the  $\text{CH}_3$  groups of the ethyls; the narrower line width is obtained by setting all those interactions to zero. The line width at 293 K (just before the transition temperature) is observed as ca. 34.6 kHz, which is similar to the calculated range.

**Phase III.** Upon the transition from phase IV to III, sudden drops in line width are observed for all nuclei: <sup>1</sup>H from 34.6 to 12.5 kHz, <sup>19</sup>F from 11.1 to 7.8 kHz, <sup>31</sup>P-cation from 8.2 to 3.0 kHz, and <sup>31</sup>P-anion from 4.4 to 3.5 kHz, as shown in Figure 9. Because the <sup>1</sup>H and <sup>31</sup>P-cation show the largest reductions in line width, and the isotropic tumbling of the anion is already underway in phase IV, it is reasonable to assume that the onset of a larger-scale motion of cations occurs as the material transforms into phase III. The most likely possibility is rotation of the entire cation around an individual axis; such behavior has also been suggested for dialkylammonium bromide plastic crystals at elevated temperature.<sup>46</sup> Calculation of the interactions with an individual  $\text{P}_{1,2,2,4}^+$  cation undergoing rotation is difficult. As a first approximation, the line widths arising from only the interionic interactions (within the 27 unit-cell block), for the case where the cation is uniaxially rotating around the  $b$  axis, have been calculated as 13.5 kHz for <sup>1</sup>H and 3.0 kHz for <sup>31</sup>P-cation (inspection of the crystal structure suggests that rotation around the  $b$  axis is less sterically hindered than rotations around other axes; calculations for rotations around other axes produced line width values within a 20% range). Both of these values are close to the measured values (especially for the <sup>31</sup>P-cation), which implies that the residual intra-cation dipole–dipole interaction must be small. This in turn suggests that in phase III extensive side-chain motions may be occurring, along with the cation rotation.

**Phase II.** The transition from phase III to II produces a dramatic narrowing of the <sup>19</sup>F and <sup>31</sup>P-anion line widths to ca. 800 Hz (narrow peak) and ca. 300 Hz, respectively. Therefore, in phase II, the anion is likely to be diffusing on the NMR time scale. In contrast, upon entering phase II, the line widths narrow gradually for both <sup>1</sup>H (from 8.6 to 5.4 kHz) and <sup>31</sup>P-cation (from 2.7 to 1.5 kHz). Thus, we believe that tumbling of the cations begins in phase II, and this tumbling is associated with the creation of significant free volume within the lattice, which in turn can facilitate the translational motion of many of the anions. These hypotheses are strongly supported by the corresponding second moment simulations. The calculated line widths for isotropically tumbling cations are 8.4 kHz for <sup>1</sup>H and 2.7 kHz for <sup>31</sup>P-cation. The gradual decrease of both <sup>1</sup>H and <sup>31</sup>P line widths within this phase is probably because the fraction of diffusive cations increases with temperature, as shown by the increasing fraction of the narrow peaks in the <sup>1</sup>H and <sup>31</sup>P-cation NMR spectra (Figure 7).

**Phase I.** As the anion reaches its diffusive state in phase II, no further significant line width narrowing for <sup>19</sup>F and <sup>31</sup>P-anion is observed in phase I (almost all <sup>19</sup>F and <sup>31</sup>P-anions are

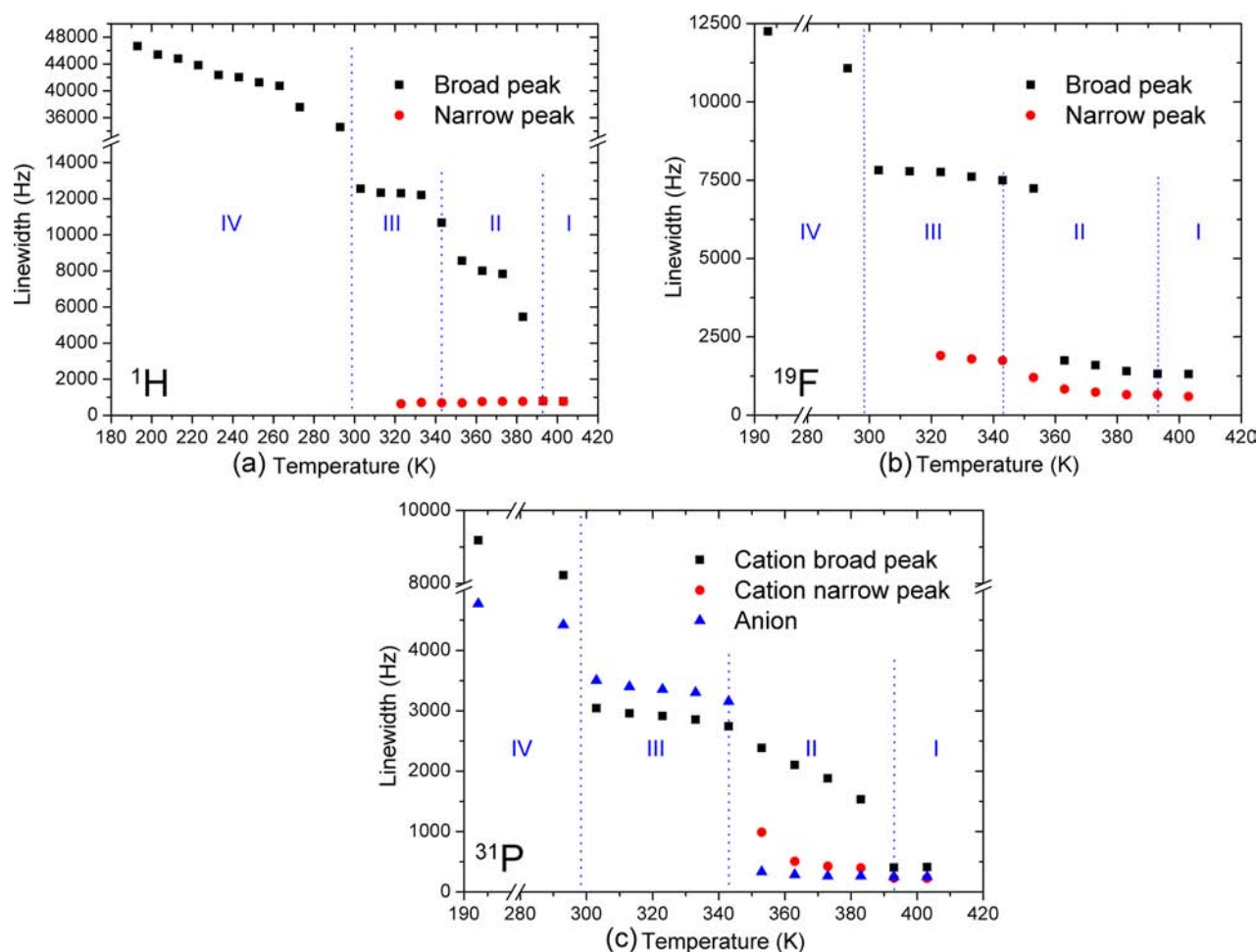


**Figure 9.** Experimental NMR line widths as a function of temperature for (a)  $^1\text{H}$ , (b)  $^{19}\text{F}$ , and (c)  $^{31}\text{P}$ . The broad peak is the original peak, and the narrow peak, due to mobile species, emerges at higher temperatures. The dashed lines indicate the transition to different phases, as determined by DSC.

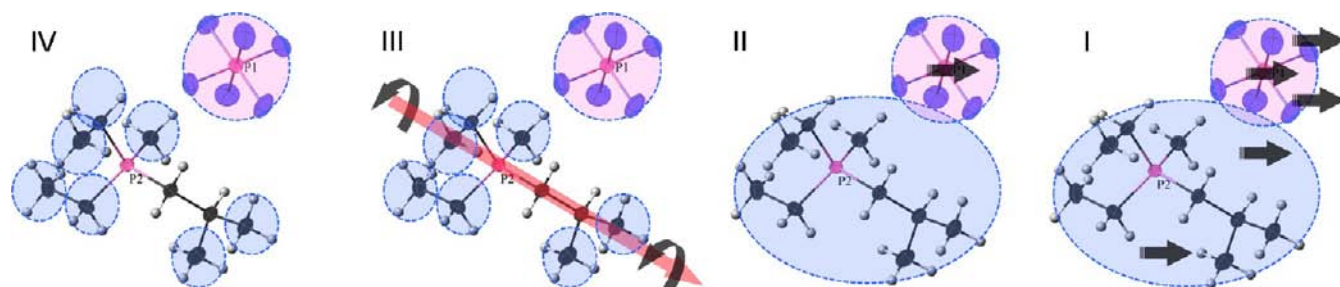


**Figure 10.** Schematic of molecular motions in different phases (IV to I) of  $[\text{P}_{1,2,2,4}][\text{PF}_6]$  with increasing temperature. Phase IV, only the methyl and ethyl groups of the cation are rotating, but the anion is tumbling (on the NMR time scale); phase III, the whole cation can rotate around one axis, and the anion continues tumbling; phase II, the whole cation can tumble, and the anion both tumbles and diffuses; phase I, both the cation and the anion can diffuse.

diffusive, with line widths ca. 650 Hz and ca. 250 Hz, respectively). Meanwhile, the transition from phase II to I allows translational motion of most of the cations, and the line widths of  $^1\text{H}$  and  $^{31}\text{P}$  drop dramatically at the transition from phase II to I (from ca. 5.4 kHz to ca. 800 Hz and from ca. 1.5 kHz to ca. 400 Hz, respectively, Figure 9). Because both cation and anion can diffuse, it is not possible to determine correlated positions of atoms. Therefore, the simulated line width is not available for this phase.

**3.5. Summary of the Transport Model.** Thus, compilation of a variety of in-depth analytical and computa-

tional techniques allows the formation of a transport model for the plastic crystal  $[\text{P}_{1,2,2,4}][\text{PF}_6]$ , as demonstrated schematically in Figure 10. In phase IV the material has an ionic conductivity below  $10^{-10} \text{ S cm}^{-1}$ , because the transport of ions is highly restricted in the relatively rigid lattice. This is consistent with the reasonably large NMR line widths measured for all nuclei. However, the isotropic tumbling of the  $\text{PF}_6^-$  anion, and some rotation of methyl and ethyl groups, do facilitate limited ion transport, albeit with a high activation energy barrier.

On the transition from phase IV to III, the ionic conductivity jumps to  $10^{-8} \text{ S cm}^{-1}$ ; this transition is also associated with

dramatic decreases in the NMR line widths of all nuclei. This is consistent with the largest transition entropy of all of the measured phase transitions, which implies that the material has become “plastic” in phase III (also confirmed from the SEM images). In this temperature range, cation rotation around the *b* axis is believed to be the predominant mechanism for reducing the energy barrier to motion of ions. Within phase III, the conductivity goes up to  $10^{-5}$  S cm<sup>-1</sup>, but none of the NMR line widths show a significant change with temperature, which suggests that the enhanced ionic conductivity arises from the defects (such as vacancies) that the motion has created. Vacancies can effectively promote the diffusive motion or hopping of ions, and reasonable diffusion coefficients for both cations and anions were observed in this phase; about 10 mol % of the anions and 1 mol % of the cations are able to diffuse, which may be a result of the channel-like crystal structure allowing the anions an easier path for diffusion.

In phase II, the isotropic tumbling of cations, with most of the anions diffusing, starts to govern the transport properties, and the conductivity increases to  $10^{-4}$  S cm<sup>-1</sup> with a small activation energy. Within this phase, the fraction of diffusive cations grows with increasing temperature, and the diffusion coefficient of those cations also gradually increases. Upon entering phase I, most cations are able to leave their lattice positions to hop and diffuse, with a diffusion coefficient of the order of  $10^{-7}$  cm<sup>2</sup> s<sup>-1</sup>, which is comparable with those of some ionic liquids.<sup>60</sup> As expected, the transport is very efficient in this phase, as the conductivity is as high as  $10^{-3}$  S cm<sup>-1</sup>. As the majority of anions are already able to diffuse on the NMR time scale, the very small ( $5$  J mol<sup>-1</sup> K<sup>-1</sup>) residual entropy of fusion is in good agreement with the highly disordered state of phase I.

#### 4. CONCLUSIONS

A comprehensive understanding of ion transport in the organic ionic plastic crystal [P<sub>1,2,2,4</sub>][PF<sub>6</sub>] has been obtained using data from a variety of experiments and also calculation of NMR line widths. The crystal structure suggests a relatively easy path for translational motion of the anions, and the slip features in the microstructure confirm that this material is plastic. The observed highly phase-dependent conductivity is consistent with the suggested transport model. In phase IV (up to 293 K), the methyl groups and ethyl groups of the cations gradually begin to rotate, and the anions tumble isotropically. The whole cation suddenly starts uniaxial rotation (possibly around the *b* axis) upon the transition from phase IV to III; this remains the dominant transport mechanism across phase III, where a minority of the anions also become diffusive because of defect formation. The whole cation begins isotropic tumbling from phase II, which allows fast diffusion of a minority of the cations and the majority of the anions (the diffusion coefficients of both ions are higher than  $10^{-11}$  m<sup>2</sup> s<sup>-1</sup>). Finally, in phase I, the conductivity reaches  $10^{-3}$  S cm<sup>-1</sup>, apparently because both the cations and the anions can diffuse in a quasi-liquid state; the residual entropy of this phase is only  $5$  J K<sup>-1</sup> mol<sup>-1</sup>, relative to the melt.

#### ■ ASSOCIATED CONTENT

##### Supporting Information

Single-crystal X-ray diffraction and structural information for [P<sub>1,2,2,4</sub>][PF<sub>6</sub>], and details of solid static NMR line width simulations by second moment calculations. This material is available free of charge via the Internet at <http://pubs.acs.org>.

#### ■ AUTHOR INFORMATION

##### Corresponding Author

jenny.pringle@monash.edu

##### Notes

The authors declare no competing financial interest.

#### ■ ACKNOWLEDGMENTS

We gratefully acknowledge funding from the Australian Research Council through its Centre of Excellence program, and also for Fellowship support for J.M.P. (QEII) and D.R.M. (Federation Fellow). We also acknowledge the use of facilities within the Monash Centre for Electron Microscopy.

#### ■ REFERENCES

- (1) Abouimrane, A.; Abu-Lebdeh, Y.; Alarco, P.-J.; Armand, M. *J. Electrochem. Soc.* **2004**, *151*, A1028.
- (2) Fan, L.-Z.; Wang, X.-L.; Long, F. *J. Power Sources* **2009**, *189*, 775.
- (3) Zhou, Q.; Boyle, P. D.; Malpezzi, L.; Mele, A.; Shin, J.-H.; Passerini, S.; Henderson, W. A. *Chem. Mater.* **2011**, *23*, 4331.
- (4) MacFarlane, D. R.; Huang, J.; Forsyth, M. *Nature* **1999**, *402*, 792.
- (5) Howlett, P. C.; Shekibi, Y.; MacFarlane, D. R.; Forsyth, M. *Adv. Eng. Mater.* **2009**, *11*, 1044.
- (6) Abouimrane, A.; Whitfield, P. S.; Niketic, S.; Davidson, I. J. *J. Power Sources* **2007**, *174*, 883.
- (7) Alarco, P.-J.; Abu-Lebdeh, Y.; Abouimrane, A.; Armand, M. *Nat. Mater.* **2004**, *3*, 476.
- (8) Alarco, P. *Solid State Ionics* **2004**, *172*, 53.
- (9) Jin, L.; Howlett, P.; Efthimiadis, J.; Kar, M.; Macfarlane, D.; Forsyth, M. *J. Mater. Chem.* **2011**, *21*, 10171.
- (10) Forsyth, M.; Huang, J.; MacFarlane, D. R. *J. Mater. Chem.* **2000**, *10*, 2259.
- (11) Sunarso, J.; Shekibi, Y.; Efthimiadis, J.; Jin, L.; Pringle, J. M.; Hollenkamp, A. F.; MacFarlane, D. R.; Forsyth, M.; Howlett, P. C. *J. Solid State Electrochem.* **2012**, *16*, 1841.
- (12) Long, S.; Howlett, P.; MacFarlane, D.; Forsyth, M. *Solid State Ionics* **2006**, *177*, 647.
- (13) Abu-Lebdeh, Y.; Abouimrane, A.; Alarco, P. J.; Hammami, A.; Ionescu-Vasii, L.; Armand, M. *Electrochem. Commun.* **2004**, *6*, 432.
- (14) Abu-Lebdeh, Y.; Abouimrane, A.; Alarco, P.-J.; Davidson, I.; Armand, M. *J. Power Sources* **2006**, *159*, 891.
- (15) Rana, U. A.; Bayley, P. M.; Vijayaraghavan, R.; Howlett, P.; MacFarlane, D. R.; Forsyth, M. *Phys. Chem. Chem. Phys.* **2010**, *12*, 11291.
- (16) Rana, U. A.; Vijayaraghavan, R.; MacFarlane, D. R.; Forsyth, M. *Chem. Commun. (Cambridge, U. K.)* **2011**, *47*, 6401.
- (17) Armel, V.; Forsyth, M.; MacFarlane, D. R.; Pringle, J. M. *Energy Environ. Sci.* **2011**, *4*, 2234.
- (18) Wang, P.; Dai, Q.; Zakeeruddin, S. M.; Forsyth, M.; MacFarlane, D. R.; Grätzel, M. *J. Am. Chem. Soc.* **2004**, *126*, 13590.
- (19) Li, Q.; Zhao, J.; Sun, B.; Lin, B.; Qiu, L.; Zhang, Y.; Chen, X.; Lu, J.; Yan, F. *Adv. Mater.* **2012**, *24*, 945.
- (20) Pringle, J. M.; Howlett, P. C.; MacFarlane, D. R.; Forsyth, M. *J. Mater. Chem.* **2010**, *20*, 2056.
- (21) Timmermans, J. *J. Phys. Chem. Solids* **1961**, *18*, 1.
- (22) MacFarlane, D. R.; Forsyth, M. *Adv. Mater.* **2001**, *13*, 957.
- (23) Dai, Q.; MacFarlane, D. R.; Howlett, P. C.; Forsyth, M. *Angew. Chem., Int. Ed.* **2005**, *44*, 313.
- (24) Hill, A. J.; Huang, J.; Efthimiadis, J.; Meakin, P.; Forsyth, M.; MacFarlane, D. R. *Solid State Ionics* **2002**, *154*, 119.
- (25) Ishida, H.; Iwachido, T.; Hayama, N.; Ikeda, R.; Terashima, M.; Nakamura, D. *Z. Naturforsch.* **1989**, *44 A*, 741.
- (26) Hattori, M.; Fukada, S. I.; Nakamura, D.; Ikeda, R. *J. Chem. Soc., Faraday Trans.* **1990**, *86*, 3777.
- (27) Ishida, H.; Matsushashi, N.; Ikeda, R.; Nakamura, D. *J. Chem. Soc., Faraday Trans. 1* **1989**, *85*, 111.
- (28) MacFarlane, D. R.; Meakin, P.; Sun, J.; Amini, N.; Forsyth, M. *J. Phys. Chem. B* **1999**, *103*, 4164.

- (29) Alarco, P.-J.; Abu-Lebdeh, Y.; Ravet, N.; Armand, M. *Solid State Ionics* **2004**, *172*, 53.
- (30) Alarco, P. J.; Abu-Lebdeh, Y.; Armand, M. *Solid State Ionics* **2004**, *175*, 717.
- (31) Armel, V.; Velayutham, D.; Sun, J.; Howlett, P. C.; Forsyth, M.; MacFarlane, D. R.; Pringle, J. M. *J. Mater. Chem.* **2011**, *21*, 7640.
- (32) Sheldrick, G. M. *Acta Crystallogr., Sect. A* **2008**, *64*, 112.
- (33) Kaplan, M. L.; Bovey, F. A.; Cheng, H. N. *Anal. Chem.* **1975**, *47*, 1703.
- (34) Massiot, D.; Fayon, F.; Capron, M.; King, I.; Le Calvé, S.; Alonso, B.; Durand, J.-O.; Bujoli, B.; Gan, Z.; Hoatson, G. *Magn. Reson. Chem.* **2002**, *40*, 70.
- (35) Stejskal, E. O.; Tanner, J. E. *J. Chem. Phys.* **1965**, *42*, 288.
- (36) Reichert, W. M.; Holbrey, J. D.; Swatloski, R. P.; Gutowski, K. E.; Visser, A. E.; Nieuwenhuyzen, M.; Seddon, K. R.; Rogers, R. D. *Cryst. Growth Des.* **2007**, *7*, 1106.
- (37) Golding, J.; Hamid, N.; MacFarlane, D. R.; Forsyth, M.; Forsyth, C.; Collins, C.; Huang, J. *Chem. Mater.* **2001**, *13*, 558.
- (38) Steiner, T. *Angew. Chem., Int. Ed.* **2002**, *41*, 48.
- (39) Efthimiadis, J.; Forsyth, M.; MacFarlane, D. R. *J. Mater. Sci.* **2003**, *38*, 3293.
- (40) Shekibi, Y.; Gray-Weale, A.; MacFarlane, D. R.; Hill, A. J.; Forsyth, M. *J. Phys. Chem. C* **2007**, *111*, 11463.
- (41) Chezeau, J. M.; Strange, J. H. *Phys. Rep.* **1979**, *53*, 1.
- (42) Rana, U. A.; Bayley, P. M.; Vijayaraghavan, R.; Howlett, P.; MacFarlane, D. R.; Forsyth, M. *Phys. Chem. Chem. Phys.* **2010**, *12*, 11291.
- (43) Annat, G.; Adebahr, J.; McKinnon, I. R.; MacFarlane, D. R.; Forsyth, M. *Solid State Ionics* **2007**, *178*, 1065.
- (44) William, D.; Callister, J. *Materials Science and Engineering: An Introduction*, 7th ed.; John Wiley & Sons, Inc.: New York, 2007.
- (45) Pringle, J. M.; Howlett, P. C.; MacFarlane, D. R.; Forsyth, M. *J. Mater. Chem.* **2010**, *20*, 2056.
- (46) Shimizu, T.; Tanaka, S.; Onoda-Yamamuro, N.; Ishimaru, S. i.; Ikeda, R. *J. Chem. Soc., Faraday Trans.* **1997**, *93*, 321.
- (47) Pringle, J. M.; Adebahr, J.; MacFarlane, D. R.; Forsyth, M. *Phys. Chem. Chem. Phys.* **2010**, *12*, 7234.
- (48) Lee, M.; Choi, U. H.; Wi, S.; Slebodnick, C.; Colby, R. H.; Gibson, H. W. *J. Mater. Chem.* **2011**, *21*, 12280.
- (49) Mehrer, H. *Diffusion in Solids*; Springer: Munster, 2007.
- (50) Annat, G.; Adebahr, J.; McKinnon, I.; Macfarlane, D.; Forsyth, M. *Solid State Ionics* **2007**, *178*, 1065.
- (51) Levitt, M. H. *Spin Dynamics: Basics of Nuclear Magnetic Resonance*, 2nd ed.; John Wiley & Sons, Ltd.: Chichester, 2008.
- (52) Van Vleck, J. H. *Phys. Rev.* **1948**, *74*, 1168.
- (53) Bayley, P. M.; Best, A. S.; MacFarlane, D. R.; Forsyth, M. *Phys. Chem. Chem. Phys.* **2011**, *13*, 4632.
- (54) Seeber, A. J.; Forsyth, M.; Forsyth, C. M.; Forsyth, S. A.; Annat, G.; MacFarlane, D. R. *Phys. Chem. Chem. Phys.* **2003**, *5*, 2692.
- (55) Petrakis, L.; Rao, A. *J. Chem. Phys.* **1963**, *39*, 1633.
- (56) Goc, R. Z. *Naturforsch., A: Phys. Sci.* **2002**, *57*, 29.
- (57) Mukhopadhyay, R. In *Solid State Physics: Proceedings of the D.A.E. Solid State Physics Symposium*; Mukhopadhyay, R., Shaikh, A. M., Godwal, B. K., Eds.; Universities Press (India) Limited: Hyderguda, 1998; Vol. 41.
- (58) Andrew, E. R. *Nuclear Magnetic Resonance*; Royal Society of Chemistry: Cambridge, 1974; Vol. 3.
- (59) Gutowsky, H. S.; Pake, G. E. *J. Chem. Phys.* **1950**, *18*, 162.
- (60) Bayley, P. M.; Lane, G. H.; Lyons, L. J.; MacFarlane, D. R.; Forsyth, M. *J. Phys. Chem. C* **2010**, *114*, 20569.